Microscopic sensors using optical wireless integrated circuits

Alejandro J. Cortese[a], Conrad L. Smart[a], Tianyu Wang[b], Michael F. Reynolds[a], Samantha L. Norris[a], Yanxin Ji[c], Sunwoo Lee[c], Aaron Mok[b], Chunyan Wu[b], Fei Xia[b], Nathan I. Ellis[a], Alyosha C. Molnar[c,d], Chris Xu[b,d], and Paul L. McEuen[a,d,1]

[a]Laboratory of Atomic and Solid State Physics, Cornell University, Ithaca, NY 14853; [b]Applied and Engineering Physics, Cornell University, Ithaca, NY 14853; [c]School of Electrical and Computer Engineering, Cornell University, Ithaca, NY 14853; and [d]Kavli Institute at Cornell for Nanoscale Science, Cornell University, Ithaca, NY 14853

This contribution is part of the special series of Inaugural Articles by members of the National Academy of Sciences elected in 2011.

Contributed by Paul L. McEuen, March 2, 2020 (sent for review November 12, 2019; reviewed by Vladimir Bulović and Michel M. Maharbiz)

We present a platform for parallel production of standalone, untethered electronic sensors that are truly microscopic, i.e., smaller than the resolution of the naked eye. This platform heterogeneously integrates silicon electronics and inorganic microlight emitting diodes (LEDs) into a 100-μm-scale package that is powered by and communicates with light. The devices are fabricated, packaged, and released in parallel using photolithographic techniques, resulting in ∼10,000 individual sensors per square inch. To illustrate their use, we show proof-of-concept measurements recording voltage, temperature, pressure, and conductivity in a variety of environments.

sensor | microscopic | microfabrication

The smallest objects resolvable by the unaided human eye are ∼100 μm in size. This limit sets a boundary between the familiar and the microscopic, the visible and invisible worlds. Driven by the expanding Internet of Things (1) and the growing deployment of implantable biomedical devices (2), researchers have created small, stand-alone, wireless electronic sensor platforms at sizes within an order of magnitude of this limit (3–16). Beginning with initial work on Smart Dust almost two decades ago (3, 4), these platforms contain silicon-based integrated circuits that are powered by and communicate through various combinations of radio frequency (RF) (5–11), batteries (6, 9, 10), ultrasound (12, 13), and light (14–16), but further progress has been slowed by challenges such as the size of RF antennas or the limits of assembly techniques such as wire bonding or wafer dicing. If such devices could be made even smaller and manufactured fully in parallel, with no dicing or manual assembly required, it would dramatically extend the range of possible applications. Such a microscopic sensor platform would be 1) nearly invisible, 2) more than 100× cheaper due to the increased number of devices per unit area, 3) deployable in ultrasmall environments, and 4) much less invasive when used as an implanted device.

Here we present a platform for building devices that match this description: microscopic, standalone, all-photolithographic optical wireless integrated circuits (OWICs). We combine silicon electronics with photovoltaics and light-emitting diodes using methods of planar heterogeneous integration, packing, and assembly. We produce OWICs as small as 0.00005 mm^3, more than a 10,000-fold reduction in volume from the mm^3 scale typical of current remotely monitored wireless technologies. The resulting OWICs are truly microscopic in size, visible to the naked eye at best as a tiny, undifferentiated speck.

Results and Discussion

Fig. 1*A* shows a complete, standalone, 8 μm × 75 μm × 175 μm OWIC on the back of a penny; it is only visible under a microscope. The mode of operation is schematically illustrated in Fig. 1*B*. When the device is illuminated: 1) Si photovoltaics provide power to the circuit, 2) n-type metal oxide semiconductor (NMOS) electronics and/or input electrodes sense a signal from the environment, and 3) a microLED communicates out the signal using light. The 2 μm-thick photovoltaics occupy less than $(50\ \mu m)^2$, and the 900-nm-thick microLED mesa used for communication occupies about $(10\ \mu m)^2$.

We choose optical input-output (I/O) because the relevant optoelectronic components can readily be miniaturized to the microscale and read out remotely using far-field, free-space coupling. In contrast, devices based $(50\ \mu m)^2$ on RF at this size (17–20) are fundamentally limited to near-field coupling, requiring readers and power sources to be within less than a millimeter of the sensors (12). Ultrasound is also emerging as a promising approach, but to date the apparatus is specialized and the sensors have not been miniaturized to truly microscopic scales (12, 13). In contrast, far-field optics is an extraordinarily well-developed and ubiquitous technology for coupling light into and out of small systems.

Fabricating OWIC sensors requires a diverse set of micro- and nanofabrication methods, as illustrated in Fig. 2 and described below (see *SI Appendix* for more details). One of the most

Significance

The smallest objects resolvable by the unaided human eye are approximately 100 μm in size. This limit sets a boundary between the familiar and the microscopic, the visible and invisible worlds. Here we describe the fabrication of tiny wireless sensors, optical wireless integrated circuits (OWICs) for optical wireless integrated circuits. OWICs are truly microscopic in size, visible to the naked eye at best as a tiny, undifferentiated speck, yet they can sense their environment and report the information back to the macroscopic world. They have potential applications in many areas of science and technology, ranging from neuroscience to chemical sensing.

Author contributions: A.J.C., A.C.M., C.X., and P.L.M. designed research; A.J.C., C.L.S., T.W., M.F.R., S.L.N., Y.J., S.L., A.M., C.W., and F.X. performed research; T.W., Y.J., S.L., A.M., C.W., F.X., N.I.E., A.C.M., and C.X. contributed new reagents/analytic tools; A.J.C., C.L.S., T.W., M.F.R., S.L.M., A.M., C.W., F.X., A.C.M., C.X., and P.L.M. analyzed data; and A.J.C., A.C.M., C.X., and P.L.M. wrote the paper.

Reviewers: V.B., Massachusetts Institute of Technology; and M.M.M., University of California, Berkeley.

Competing interest statement: A.J.C, S.L., A.C.M., and P.L.M. have filed a Patent Cooperation Treaty application that covers the work reported here (Provisional Patent Application 62/740,326).

See Profile on page 9142.

[1]To whom correspondence may be addressed. Email: plm23@cornell.edu.

This article contains supporting information online at https://www.pnas.org/lookup/suppl/doi:10.1073/pnas.1919677117/-/DCSupplemental.

First published April 17, 2020.

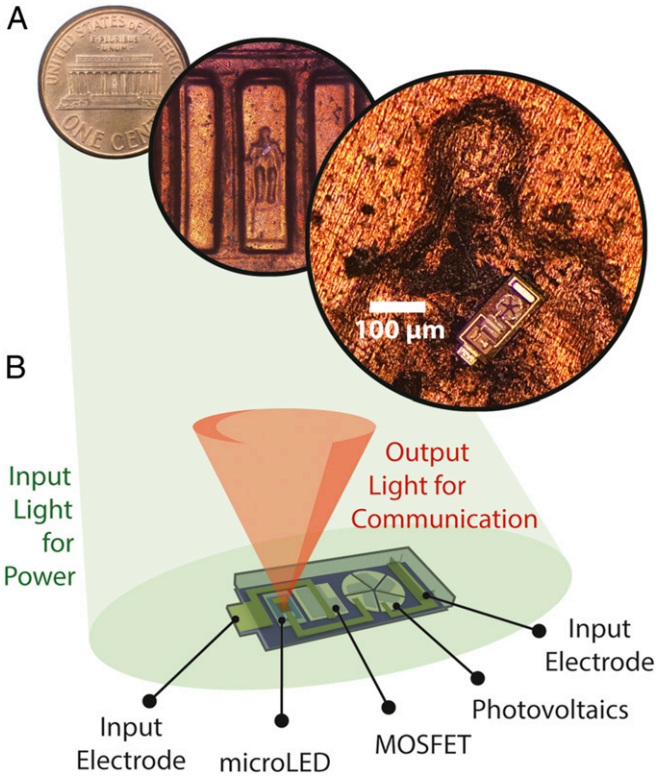

Fig. 1. Microscopic OWICs. (*A*) Optical micrograph of a voltage-sensing OWIC on the back of a penny. It is essentially invisible to the naked eye. (*B*) Schematic of OWIC in operation. Optical communication and optical power are combined with electronics into a fully integrated, microscopic sensor package.

challenging fabrication steps is the incorporation of microLEDs. There has been extensive work to integrate silicon and GaAs components in the past (21–24), including elastomer stamp transfer (21). We developed an alternative method illustrated schematically in Fig. 2 *A*–*D* that builds on this previous work while having favorable advantages for our fabrication process by 1) avoiding the need for using breakaway tethers to the prefabricated microLEDs (21, 24), and 2) not requiring adhesion layers on the transfer substrate prior to transfer (21, 24). The latter in particular would both increase topography and limit the temperature budget in subsequent processing.

The microLED integration process is shown in Fig. 2 *A*–*E*. First, GaAs LED heterostructures were epitaxially grown by a commercial vendor using metal-organic chemical vapor deposition (MOCVD) on an $Al_{0.9}Ga_{0.1}As$ etch stop layer which was itself grown on a thick GaAs substrate. MicroLEDs are then fabricated using standard photolithography and semiconductor processing. Polymethyl methacrylate (PMMA) is then spun onto the substrate and cured (Fig. 2*A*). The substrate is then submerged into a citric acid and hydrogen peroxide mixture (Fig. 2*B*), which selectively removes the GaAs substrate with negligible etching of the $Al_{0.9}Ga_{0.1}As$ etch-stop layer. The PMMA serves as a protective coating for the microLEDs during this etch step. The etch-stop layer is then selectively removed with dilute hydrofluoric acid (Fig. 2*C*). The polymer film containing microLEDs is then (Fig. 2*D*) transferred to a silicon-on-insulator (SOI) substrate. Prior to transfer, dopants were diffused and activated in the device layer of the SOI to form a p–n junction. Activating the dopants prior to transfer avoids exposing the microLEDs to damaging high temperatures. The PMMA film is then etched away via reactive-ion etching (RIE) and the microLEDs are pinned to the substrate with conformal oxide (Fig. 2*E*).

Since there is a uniform silicon p–n junction everywhere on the SOI substrate—with dopants already activated during the earlier high-temperature anneal—this method enables the subsequent fabrication of electronics in alignment with the transferred microLEDs (Fig. 2 *E*–*G*). By etching to the appropriate layers in this p–n junction and making electrical contact, we produce photovoltaics and n-channel vertical metal-oxide-semiconductor field-effect transistors (MOSFETs). A subsequent photolithography step is used to electrically connect the Si electronics and the GaAs microLEDs. This LED-first approach simplifies the transfer process by not requiring alignment of the microLEDs to preexisting microscale components. Further, this fully parallel heterogeneous integration results in OWICs with sizes and densities that would be unattainable with other interconnect techniques such as wire bonding.

In the final fabrication steps, the devices are encapsulated in SU-8 and SiO_2 and prepared for release. Openings are made in the buried oxide layer of the SOI substrate around the OWICs using RIE, leaving the thermal oxide under the OWICs to serve as a bottom encapsulation layer. Thin aluminum strips are then patterned to temporarily hold the OWICs during later processing steps. SU-8 is then patterned on top of OWICs to serve as a top encapsulation layer as shown schematically in Fig. 2*F*. An optical image of an OWIC prior to xenon difluoride (XeF_2) etching is shown in Fig. 2*H* with components labeled.

The silicon substrate underneath the OWICs is then etched away with XeF_2, which has high selectivity against etching of the encapsulation layers, protecting the silicon electronics of the OWICs. At this point, OWICs are completed and held to the substrate only by aluminum release tags, as illustrated schematically in Fig. 2*G*. Fig. 2*J* shows optical images of various OWIC designs following XeF_2 etching.

The integration, packaging, and assembly of OWICs takes place in massive parallel, producing thousands of devices per square inch (Fig. 2*I*). Approximately 3 million OWICs could fit on a single commercial 8-in. wafer, making the price per sensor less than 1 cent assuming standard complementary metal oxide semiconductor (CMOS) foundry manufacturing costs (25). Designs are also not limited to one configuration on each substrate. The OWICs platform can be customized for many possible applications; any silicon-based circuit or sensor consisting of p–n junctions and NMOS electronics can be realized.

The completed OWICs, held only by the release tags, can easily be released from the bulk substrate and placed/dispersed as detailed in Fig. 3. One method involves releasing OWICs into solution. The aluminum release tags are designed to be selectively etched in dilute tetramethylammonium hydroxide without damaging the OWICs. The OWICs can then be diluted into water allowing for many modes of delivery including syringe injection, polymer embedding, and aerosolization (Fig. 3 *A*–*C*) that would be impossible for larger sensors (26–28). Alternately, OWICs can be directly removed from the substrate using a glass micropipette and precisely placed onto a target substrate (Fig. 3 *D*–*J*). This method closely resembles that used in standard, commercially available, pick-and-place machines. For biological applications requiring devices to be inserted into tissue, Fig. 3 *K*–*N* details a pair of micromachined silicon microneedles that can controllably deliver devices into tissue (see *SI Appendix* for more details). Fig. 3*N* demonstrates these microneedles being used to insert an OWIC sensor into the brain tissue of a mouse, as discussed further below.

The function of voltage-sensing OWICs is shown in Fig. 4. The sensor is remotely powered with a 532-nm laser, which is coupled into a microscope objective to achieve full field-of-view illumination. This light drives the *n* photovoltaics (PVs) in series, each of which outputs at approximately their open-circuit voltage V_{oc}. For sufficient input

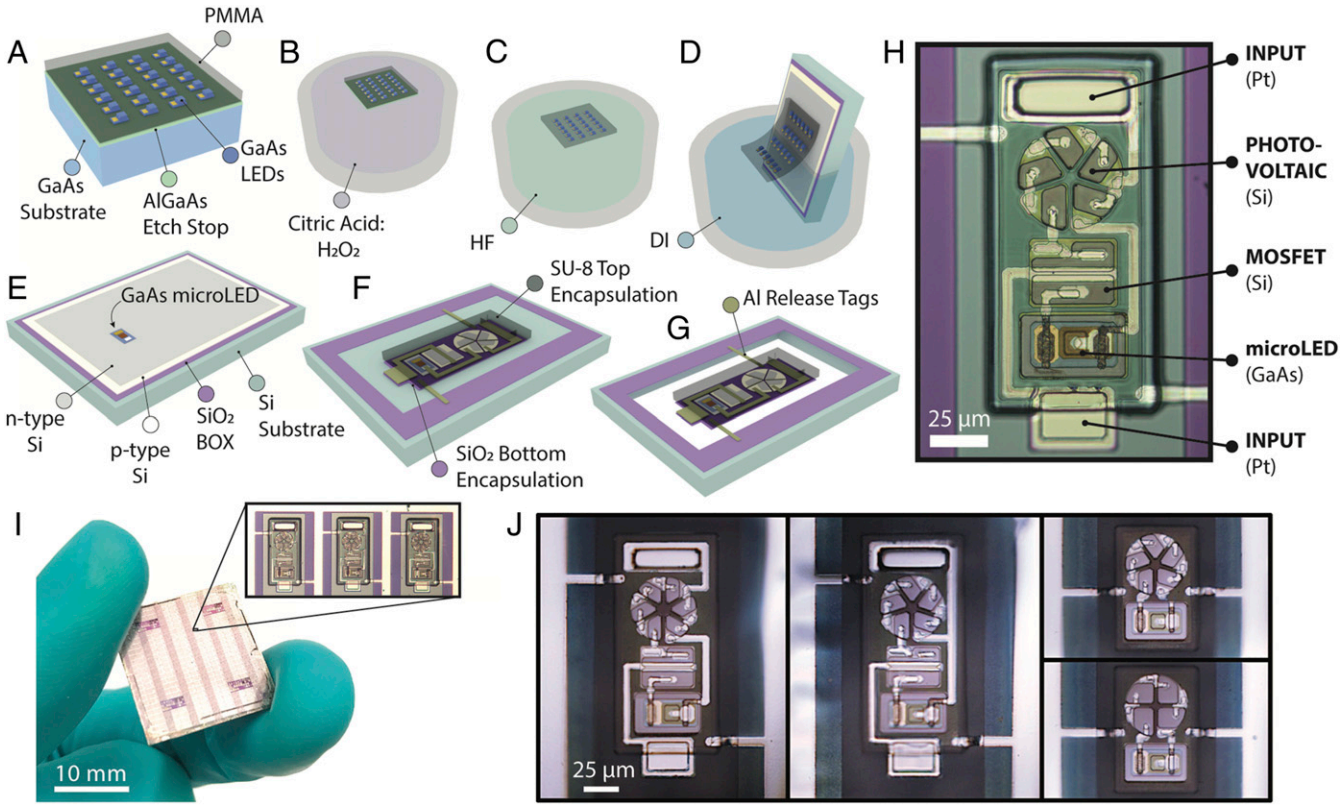

Fig. 2. Parallel fabrication of OWICs. (*A*) Prepatterned GaAs microLEDs grown on an $Al_{0.9}Ga_{0.1}As$ etch-stop layer are embedded in spun-on PMMA. The GaAs substrate and the $Al_{0.9}Ga_{0.1}As$ etch stop are then selectively etched (*B* and *C*). The PMMA containing GaAs microLEDs is then (*D*) transferred onto (*E*) an SOI substrate containing a p–n junction. PMMA is then removed via dry etching and microLEDs are pinned to the substrate with a thin conformal oxide layer. (*F*) Silicon photovoltaics, vertical MOSFETs, and electrical interconnects are then patterned photolithographically along with SU-8 and SiO_2 encapsulation layers for packaging. (*G*) The substrate silicon below the device is then selectively etched away with OWICs only tethered to the substrate with thin aluminum release tags. (*H*) Optical image of an OWIC sensor with components labeled (before substrate etching). (*I*) Image of a chip containing thousands of integrated OWICs. (*J*) Image of various OWIC sensors suspended by breakaway tags after the substrate beneath them was etched away.

optical power, the total applied voltage nV_{oc} driving the circuit is relatively constant, providing isolation from noise/variations in the illumination conditions (see details in *SI Appendix*, Fig. S11).

The voltage from the PVs drives the series combination of the MOSFET and the microLED (Fig. 2*H*). The resulting output light, centered at 840 nm, is then collected into the microscope objective and monitored using a silicon photodetector (*SI Appendix*, Fig. S6). The objective was 5 mm away in these experiments to maximize the signal, but longer working distances were also routinely used.

The measured power output of the microLED versus the voltage across its input electrodes is shown in Fig. 4*B*. Changes in the input voltage modulate the MOSFET current, which changes the amount of light output. This peaks around zero bias, with a normalized change of $S_V = (dP/dV)/P = 2.3 \times 10^{-3}/\text{mV}$. The voltage sensitivity S_V is comparable for different OWICs, with 10% variations typical. For small voltage changes ($\sim^{+/-}100$ mV), the measured voltage is thus given by

$$\Delta V(t) = \frac{1}{S_V}\left(\frac{\Delta P(t)}{P}\right),$$

where $\Delta P/P$ is the measured percentage change in the output optical signal at a given time (more details on calibration are available in *SI Appendix*).

Note that the measured voltage depends on normalized changes in the output light, not the absolute magnitude of the signal itself. In addition, variations in the input light do not significantly affect the drive, as discussed above. This makes the accurate measurement of short-term voltage changes fairly robust against the details of the optical path and also gradual changes in the illumination/collection conditions.

The device shown has a voltage resolution of 8 μV $Hz^{-1/2}$ when operated under continuous illumination, operates at speeds greater than 10 kHz, and consumes ~60 μW of power. To reduce power consumption, it can be measured at low duty cycles, albeit with a correspondingly degraded noise performance. Fig. 4*C* shows a voltage-sensing OWIC operated with a 30% duty cycle, reducing the average power to 18 μW. For 1-μW average power, the voltage sensitivity is still less than 0.1 mV $Hz^{-1/2}$. While the voltage resolution of these proof-of-concept sensors is more than adequate for many applications, it is not sensitive enough to detect, e.g., neural activity. However, more sophisticated circuits can be incorporated in future generations to improve resolution (15). See *SI Appendix*, Fig. S10 for more details on the noise spectra.

Fig. 4*D* shows a voltage-sensing OWIC used to measure local conductivity of water in a sealed microfluidic channel, relevant for applications including single-cell sorting (29) and desalination of sea water (30). When a known fixed current is run through the microfluidic channel, the voltage drop across the OWIC is directly proportional to the solution conductivity. Fig. 4*D* shows real-time optical recordings of a voltage-sensing OWIC in a sealed 50 μm × 200 μm polydimethylsiloxane channel initially containing a low concentration solution of potassium chloride (KCl). Small volumes of higher concentration KCl are subsequently added to a nearby reservoir and diffuse into the channel. Measured conductivities of 2.2, 17.7, and 165.9 mS cm^{-1}

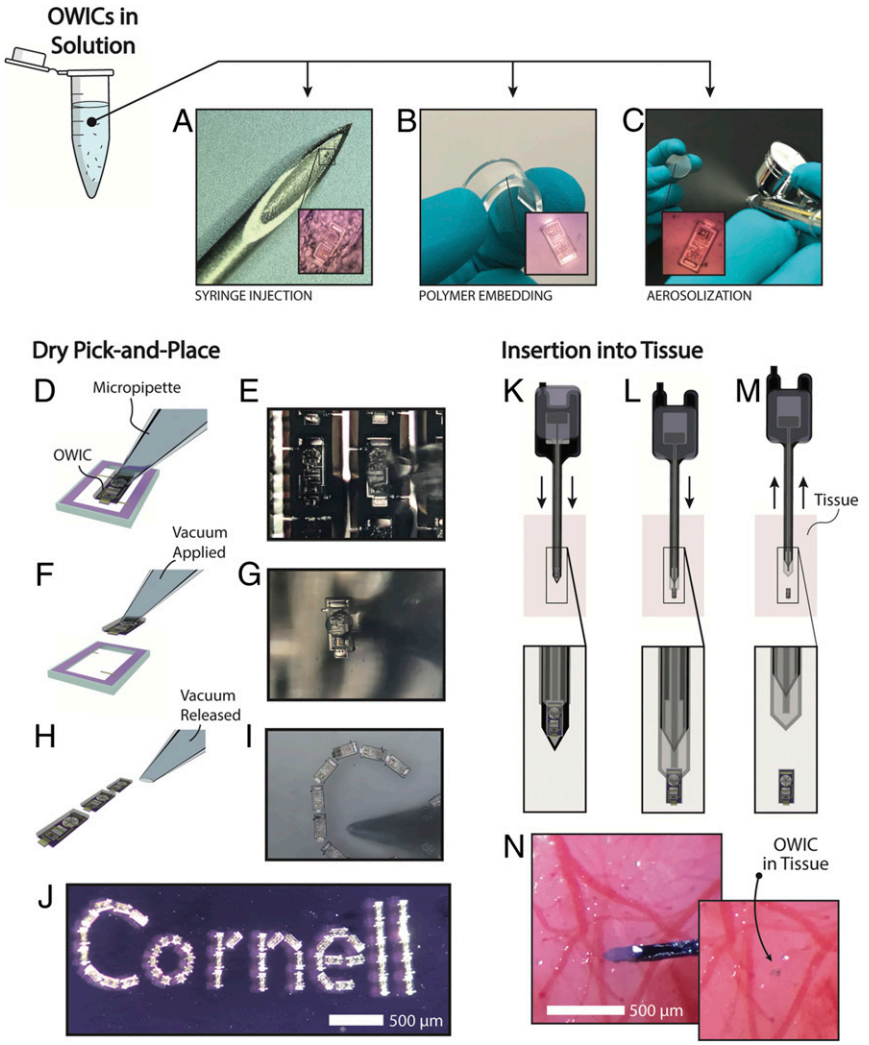

Fig. 3. Manipulation and delivery Modes. (*A*–*C*) OWICs can be released in solution for subsequent (*A*) syringe injection, (*B*) embedding in a flexible polymer, or (*C*) aerosolization onto a substrate. (*D*–*J*) Dry pick-and-place of OWICs using a glass micropipette. Schematic and optical images of (*D* and *E*) a glass micropipette coming into contact with an OWIC that is still tethered to the bulk substrate with aluminum release tags, (*F* and *G*) applying vacuum to remove the OWIC from the bulk substrate, and (*H* and *I*) releasing the OWIC in a precise location and orientation on another substrate. (*J*) OWICs placed precisely into the Cornell logo on a glass slide. (*K*–*N*) Method for inserting OWICs into tissue with controlled position and orientation using a pair of custom microneedles that can slide with respect to one another. Schematic of the insertion process: (*K*) the pair of microneedles holds the OWIC as it is inserted into tissue, (*J*) the top microneedle and its extruded post push the OWIC to a particular location, and (*M*) the microneedles are removed from tissue leaving the OWIC. (The microneedles are detailed in *SI Appendix, Supplementary Materials*.) (*N*) Optical image of an OWIC inserted into the brain of a living mouse using the custom microneedles (*Left*) and image of the device after the microneedles has been removed (*Right*).

closely match the values 2.1, 17.8, and 142.7 mS cm^{-1} of the input solutions measured with a commercial instrument. The average power consumption of the OWIC was ∼10 µW. The average input power of light incident on the photovoltaics was ∼80 µW, indicating an optical power link efficiency of ∼12% (or 0.2% if considering the 6 mW delivered to the full field of view).

Fig. 5 shows the operation of temperature-sensing OWICs. They are composed of silicon photovoltaics in series with a GaAs microLED in a package 8 µm × 65 µm × 100 µm (Fig. 5*A*). The dependence of power output on temperature is shown in Fig. 5*B* and is given by

$$\Delta T(t) = \frac{1}{S_T}\left(\frac{\Delta P(t)}{P}\right),$$

where $S_T = 2 \times 10^{-2}$/K and varies from device to device by less than 5%. This is due to the well-known decrease of V_{oc} with increasing temperature predominantly caused by the temperature dependence of the intrinsic carrier density and silicon's band gap (31). As was the case for voltage-sensing OWICs, the output signal is relatively insensitive to input power variations for intensities at or above 300 nW μm^{-2} (*SI Appendix*).

Fig. 5*C* shows a temperature-sensing OWIC in operation: current pulses are run through a nearby resistor producing quick Joule heating that is recorded by the OWIC. The sensitivity in this measurement is 3 mK $Hz^{-1/2}$ averaged over a bandwidth of 1 kHz. Power requirements for operation are comparable to the voltage-sensing OWICs described above (details in *SI Appendix*).

These OWICs can also probe thermal conductivity and heat capacity at the microscale. Fig. 5*D* shows optical recordings from temperature-sensing OWICs in different environments, including air at atmospheric and low pressure (800 mTorr) and water. At time 0, an average light intensity of ∼100 nW μm^{-2}—500-nW μm^{-2} peak intensity power with 20% duty cycle—is turned on to both power

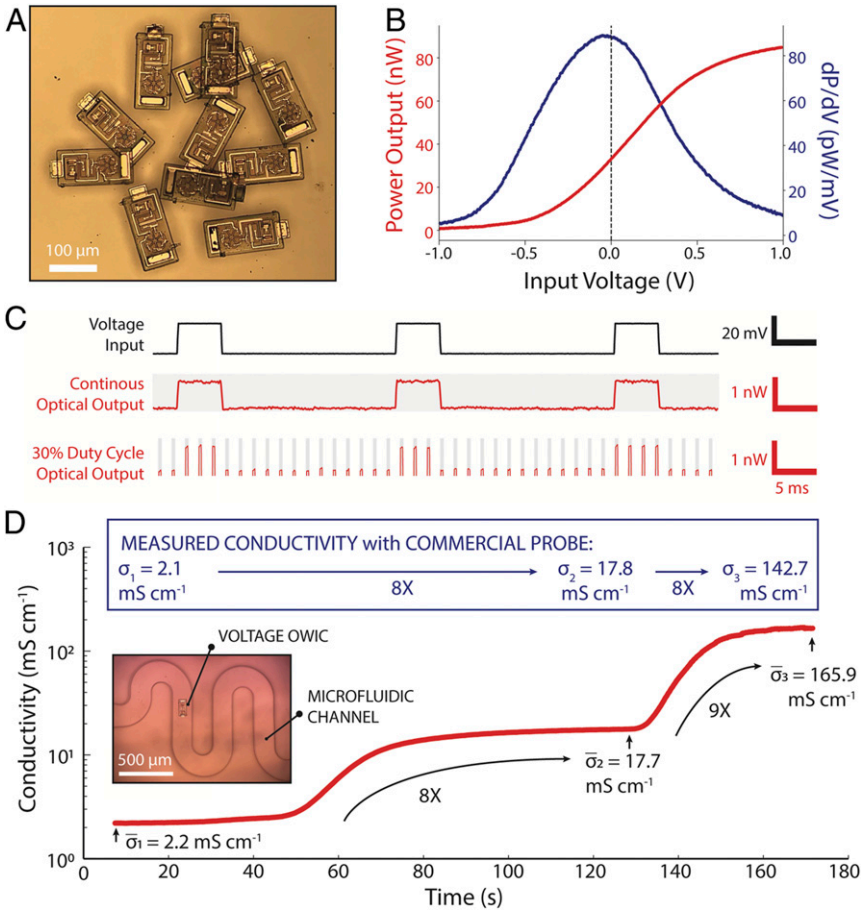

Fig. 4. Voltage-sensing OWICs. (*A*) Image of released voltage-sensing OWICs. (*B*) Characteristics of optical power output as a function of voltage applied to the input electrodes. (*C*) A 20-mV input voltage pulse (black) and the corresponding optical recording from the voltage-sensing OWIC (red) operated under continuous and pulsed input power. Regions are shown with a gray background when the light providing power to the OWIC is on. (*D*) Local solution conductivity as measured optically from a voltage-sensing OWIC inside of a sealed 50 μm × 200 μm microfluidic channel containing a KCl solution. As higher concentrations of KCl diffuse into the microfluidic system and a known current is supplied through the channel, the OWIC measures the transitions from low to high conductivity, closely matching measurements with an external commercial probe (blue box). (*Inset*) Optical image of the OWIC in the microfluidic channel.

and heat the device. As the device heats, the temperature is monitored in real time with millisecond resolution. The response is fit with an exponential with time constant $\tau = C/G$, where C and G are, respectively, the effective thermal conductance and heat capacity of the sensor and its environment. This time also sets the fastest response time for the sensor, which, based on the above equation, scales as the square of the size of the sensor. A 100-μm OWIC sensor is therefore 100× faster than a millimeter-scale device.

The initial rate of heating dT/dt and steady-state temperature change ΔT allow us to determine C and G separately: $C = P_{abs}/(dT/dt)$ and $G = P_{abs}/\Delta T$ where P_{abs} is the absorbed power. For example, in air, the inferred heat capacity is $C \sim 10^{-7}$ J K^{-1} and thermal conductance $G \sim 25$ μW K^{-1}, consistent with the known size of the OWIC sensor and the thermal conductance of air (*SI Appendix*). When the OWIC is surrounded by water, the temperature change is smaller due to the higher thermal conductivity of water, in agreement with simple estimates (*SI Appendix*).

In the future, we envision that temperature-sensing OWICs can be used to probe a variety of small samples, e.g., 100-μm-sized microcrystals of quantum materials to measure their heat capacity and thermal conductance. Such measurements are difficult now because of the large thermal mass of traditional sensors obscuring the signal from the sample itself.

Temperature-sensing OWICs can additionally be used to monitor the pressure of a gas environment, since at small scales the effective thermal conductivity of gases varies with pressure (32). Fig. 5*E* shows the output light power and extracted ΔT from a temperature-sensing OWIC inside a sealed vacuum chamber. As pressure changes, the steady-state temperature change is optically recorded from the outside of the chamber through a high-vacuum window. Using this OWIC sensor, we measure pressure with a sensitivity of approximately $\Delta P/P = 10^{-3}$ at 10-Hz bandwidth over the range shown. The device is operated with low duty cycle, consuming an average power of 10 μW, and it occupies a space no larger than a grain of dust. These wireless, optical recordings of pressure have many potential applications in micro-electromechanical systems, microelectronics, and laboratory-on-a-chip systems where devices are often hermetically sealed in vacuum and a method of remotely monitoring pressure in the microscale environment is desirable (32, 33).

OWICs also hold great potential as embedded sensors in living organisms. An in vivo multiphoton three-dimensional (3D) image of the temperature-sensing OWIC in a living mouse brain is shown in Fig. 5*F*. Both the device and surrounding vasculature of the brain are clearly visible. The custom silicon microneedles detailed in Fig. 3 *K*–*N* were used to insert and deliver the OWIC, in this case to a depth of 160 μm in the brain. The cross-section

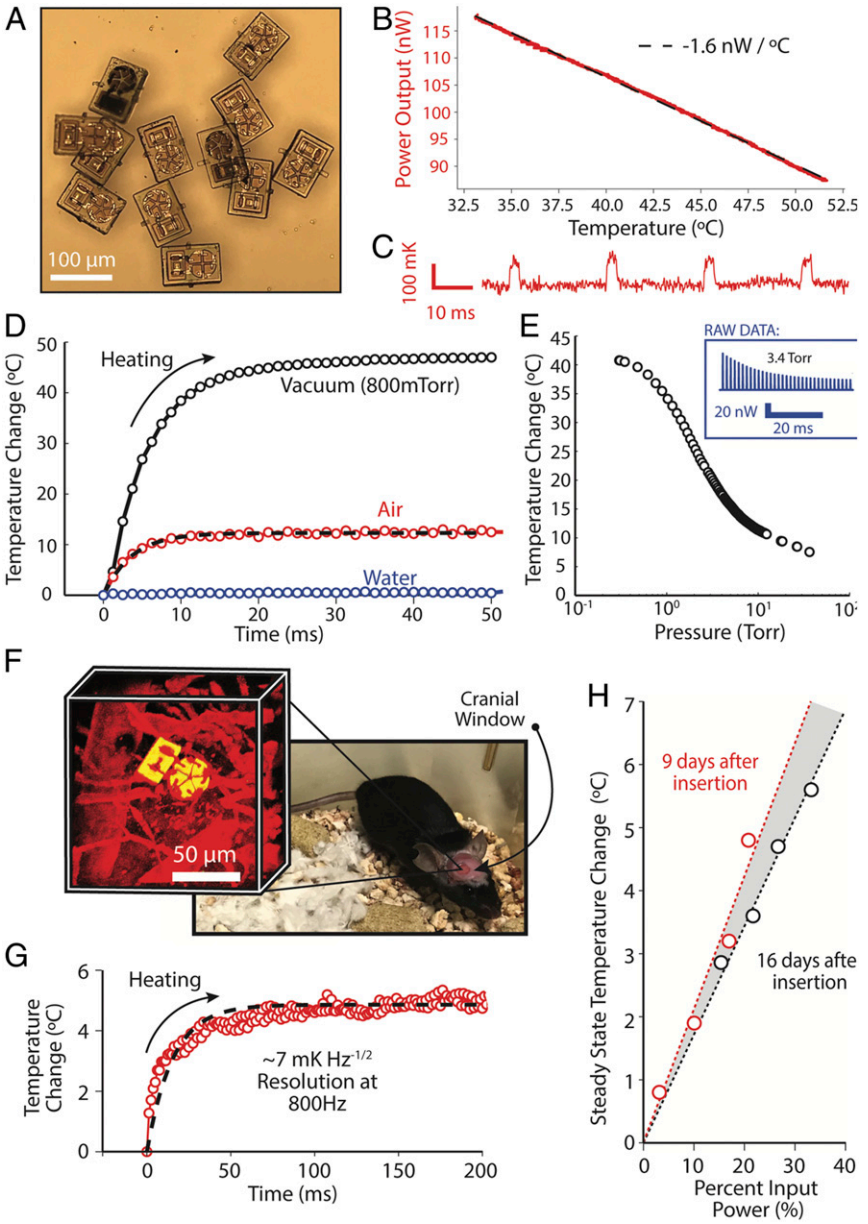

Fig. 5. Temperature-sensing OWICs. (*A*) Image of released, temperature-sensing OWICs. (*B*) Characteristics of optical power output as a function of temperature. (*C*) Measurement of small, rapid temperature changes caused by a resistive element placed next to the temperature sensor (see *SI Appendix, Supplementary Materials*). (*D*) Optical recordings from OWICs in water (blue), air (red), and vacuum (black) after a fixed intensity input power was turned on at time 0. Dashed line is an exponential fit to the response in air. (*E*) Steady-state temperature from a temperature-sensing OWIC sensor in a sealed vacuum chamber for various pressures. (*Inset*) Raw optical recording of power output at 3.4 Torr for low duty-cycle input power. (*F*) A 3D reconstruction of the implanted OWIC and vasculature in the mouse brain. Blood vessels labeled with fluorescein and imaged by three-photon microscopy with 1,320-nm excitation (red). Implanted OWIC visualized by label-free third harmonic generation by the same 1,320-nm beam (yellow). The device is nominally 160 μm into the brain. (*Right*) Image of mouse after insertion with a transparent cranial window installed for imaging. (*G*) Optical recording of temperature from the OWIC sensor monitored in vivo as the input power was used to heat the device and surrounding tissue. A temperature noise floor of 7 mK Hz$^{-1/2}$ in an 800-Hz bandwidth is observed. Dashed line indicates exponential fit of data. (*H*) Long-term optical measurements of steady-state temperature change as a function of average input power (adjusted through duty cycle) for 9 and 16 d after insertion. Linear fits shown in dashed lines.

of the insertion assembly is 45 μm × 95 μm, allowing for minimally invasive delivery. Furthermore, no tethered components remain following removal of the silicon microneedle. After surgery, a transparent cranial window (Fig. 5*F*) was installed to allow optical imaging and monitoring of the OWIC sensor, a standard method for chronic optical measurements.

The OWIC was then used to monitor local temperature changes in vivo. Understanding local temperature changes in the brain is important in, e.g., optogenetics applications, where excessive optically induced heating can damage tissue. As shown in Fig. 5*G*, an external pulsed laser both intentionally self-heats and powers the temperature-sensing OWIC. This measurement allows for monitoring 1) the response time of the OWIC-tissue system, 2) the steady-state temperature change, and 3) the in vivo temperature resolution, all from a distance of ∼5 mm. We measure a resolution of 7 mK Hz$^{-1/2}$ and temperature changes as fast as 10^3 K s^{-1} monitored with periodic sampling at 800 Hz. We find a thermal time constant of 10 ms, consistent

with expectations from the heat capacity and thermal conductivity of the device and the surrounding media. Such rapid measurements would not be achievable with macroscale temperature sensors and their larger heat capacities.

The above results only hint at the possibilities of microscopic, optical wireless electronic sensors in biological systems. Extensive further work will be required to fully address biocompatibility, expected device lifetime, depth of light penetration, and other challenges specific to each targeted application. For example, any future applications in vivo will have to address signal degradation due to absorption and scattering, likely with completely intensity-independent I/O such as pulse-position modulation (15). But, the possibility of recording temperature, voltage, etc. using a wireless sensor no larger than a large cell has the potential to be broadly impactful.

The OWIC platform described here pushes wireless sensors to the truly microscopic scale. The sensors are first generation and proof of concept, but the platform can readily be expanded to include more complex NMOS and CMOS circuitry in the future. Improved design and efficiency will also lead to more broadly applicable OWICs. Specifically, lower power consumption, improved communication protocols, and even longer read distances could result from exploring pulsed low duty-cycle power schemes (15), differential, radiometric measurement of two different wavelength microLEDs (34), and narrow-wavelength, collimated vertical-cavity surface-emitting lasers (35), respectively. Potential future applications include wireless neural recording with a sensor so small as to avoid scarring, to heat-capacity measurements of samples too small to be otherwise measured, to wireless sensors providing quantitative information inside of microfluidic systems. We emphasize that OWICs are a general platform for microscopic I/O, and any of the plethora of microscale electronic sensors fabricated using standard lithographic techniques can readily be integrated.

Materials and Methods

The AlGaAs/GaAs heterostructure used for producing transferrable LEDs was epitaxially grown by MOCVD by a commercial vendor (Matrix Opto. Co., Ltd). The SOI substrate used for fabrication of microelectronics was produced by a commercial vendor (Ultrasil Corporation) and consists of a <100> p-type (boron doped) 2-μm device layer and a 500-nm buried oxide layer on a thick silicon handle. Other than the microLED transfer method described above, standard semiconductor processing was used for the patterning of microLEDs and silicon electronics. In all optical measurements, a wavelength of 532 nm was coupled into a microscope and used to power OWICs. The output OWIC signal centered at 840 nm was then collected into the microscope objective, selectively filtered, and focused onto a photodetector that was read out using a digital oscilloscope. Detailed methods are provided in *SI Appendix*. All animal experiments and housing procedures were conducted in accordance with Cornell University Institutional Animal Care and Use Committee guidance.

Data Availability Statement. All data for this paper are available in the main text and *SI Appendix*.

ACKNOWLEDGMENTS. We thank M. Miskin, K. Dorsey, M. Velicky, and the Cornell Nanoscale Facility staff members for fruitful discussions. This work was supported by the Cornell Center for Materials Research with grant funding from the NSF Materials Research Science and Engineering Center (MRSEC) program (DMR-1719875), by the Air Force Office of Scientific Research (Multidisciplinary University Research Initiative: FA9550-16-1-0031), and by the Kavli Institute at Cornell for Nanoscale Science. Additional grant funding was provided by National Institute of Health Department of Health and Human Services (U01 NS107687 and R21 EY027581). A.J.C. acknowledges support by the National Science Foundation Graduate Research Fellowship (DGE-1650441). This work made use of the NSF-supported Cornell Nanoscale Facility (ECCS-1542081) and the Cornell Center for Materials Research Shared Facilities, which are supported through the NSF MRSEC Program (DMR-1719875).

1. A. Al-Fuqaha, M. Guizani, M. Mohammadi, M. Aledhari, M. Ayyash, Internet of Things: A survey on enabling technologies, protocols, and applications. *IEEE Comm. Surv. and Tutor.* **17**, 2347–2376 (2015).
2. K. Agarwal, R. Jegadeesan, Y.-X. Guo, N. V. Thakor, Wireless power transfer strategies for implantable bioelectronics. *IEEE Rev. Biomed. Eng.* **10**, 136–161 (2017).
3. J. M. Kahn, R. H. Katz, K. S. J. Pister, "Next century challenges: Mobile networking for 'smart dust" in *Proceedings of the 5th Annual ACM/IEEE International Conference on Mobile Computing and Networking* (ACM, New York, 1999) pp. 271–278.
4. B. Warneke, M. Last, B. Liebowitz, K. S. J. Pister, "Smart Dust": Communicating with a cubic-millimeter computer. *Computer* **34**, 44–51 (2001).
5. W. Biederman *et al.*, A fully-integrated, miniaturized (0.125 mm^2) 10.5 μW wireless neural sensor. *IEEE J. Solid-State Circuits* **48**, 960–970 (2013).
6. G. Chen *et al.*, "A cubic-millimeter energy-autonomous wireless intraocular pressure monitor" in *Solid-State Circuits Conference Digest of Technical Papers (ISSCC), 2011 IEEE International* (IEEE, New York, 2011), pp. 310–312.
7. R. Harrison *et al.*, "A low-power integrated circuit for a wireless 100-electrode neural recording system" in *2006 IEEE International Solid State Circuits Conference–Digest of Technical Papers* (IEEE, San Francisco, CA, 2006), pp. 2258–2267.
8. J. S. Ho *et al.*, Wireless power transfer to deep-tissue microimplants. *Proc. Natl. Acad. Sci. U.S.A.* **111**, 7974–7979 (2014).
9. S. Jeong *et al.*, A fully-integrated 71 NW CMOS temperature sensor for low power wireless sensor nodes. *IEEE J. Solid-State Circuits* **49**, 1682–1693 (2014).
10. Y. Lee *et al.*, A modular 1 mm^3 die-stacked sensing platform with low power I^2C inter-die communication and multi-modal energy harvesting. *IEEE J. Solid-State Circuits* **48**, 229–243 (2013).
11. P. Yeon, S. A. Mirbozorgi, B. Ash, H. Eckhardt, M. Ghovanloo, Fabrication and microassembly of a mm-sized floating probe for a distributed wireless neural interface. *Micromachines (Basel)* **7**, E154 (2016).
12. D. Seo *et al.*, Wireless recording in the peripheral nervous system with ultrasonic neural Dust. *Neuron* **91**, 529–539 (2016).
13. J. Charthad, M. J. Weber, C. C. Ting, A. Arbabian, A mm-sized implantable medical device (IMD) with ultrasonic power transfer and a hybrid Bi-directional data link. *IEEE J. Solid-State Circuits* **50**, 1741–1753 (2015).
14. S. Ayazian, V. A. Akhavan, E. Soenen, A. Hassibi, A photovoltaic-driven and energy-autonomous CMOS implantable sensor. *IEEE Trans. Biomed. Circuits Syst.* **6**, 336–343 (2012).
15. S. Lee *et al.*, A 250 μm × 57 μm microscale opto-electronically transduced electrodes (MOTEs) for neural recording. *IEEE Trans. Biomed. Circuits Syst.* **12**, 1256–1266 (2018).
16. B. A. Warneke *et al.*, "An autonomous 16 mm^3/solar-powered node for distributed wireless sensor networks" in *2002 Proceeding of IEEE SENSORS* (IEEE, New York, 2002), vol. 2, pp. 1510–1515.
17. L. Y. Chen *et al.*, Mass fabrication and delivery of 3D multilayer μTags into living cells. *Sci. Rep.* **3**, 2295 (2013).
18. X. Hu *et al.*, Micrometer-scale magnetic-resonance-coupled radio-frequency identification and transceivers for wireless sensors in cells. *Phys. Rev. Appl.* **8**, 014031 (2017).
19. P. Ralston *et al.*, Defeating counterfeiters with microscopic dielets embedded in electronic components. *Computer* **49**, 18–26 (2016).
20. M. Usami, "The world's smallest RFID chip technology" in *Analog Circuit Design*, H. Casier, M. Steyaert, A. H. M. van Roermund, Eds. (Springer Netherlands, Dordrecht, 2011), pp. 277–287.
21. S. I. Park *et al.*, Printed assemblies of inorganic light-emitting diodes for deformable and semitransparent displays. *Science* **325**, 977–981 (2009).
22. E. Yablonovitch, T. Gmitter, J. P. Harbison, R. Bhat, Extreme selectivity in the lift-off of epitaxial GaAs films. *Appl. Phys. Lett.* **51**, 2222–2224 (1987).
23. E. Yablonovitch, D. M. Hwang, T. J. Gmitter, L. T. Florez, J. P. Harbison, Van der waals bonding of GaAs epitaxial liftoff films onto arbitrary substrates. *Appl. Phys. Lett.* **56**, 2419–2421 (1990).
24. J. Justice *et al.*, Wafer-scale integration of group III–V lasers on silicon using transfer printing of epitaxial layers. *Nat. Photonics* **6**, 610–614 (2012).
25. K. Flamm, "Measuring Moore's Law: Evidence from Price, Cost, and Quality Indexes." Working Paper. National Bureau of Economic Research, April 2018. http://www.nber.org/papers/w24553.pdf.
26. J. Liu *et al.*, Syringe-injectable electronics. *Nat. Nanotechnol.* **10**, 629–636 (2015).
27. M. A. Meitl *et al.*, Transfer printing by kinetic control of adhesion to an elastomeric stamp. *Nat. Mater.* **5**, 33–38 (2006).
28. V. B. Koman *et al.*, Colloidal nanoelectronic state machines based on 2D materials for aerosolizable electronics. *Nat. Nanotechnol.* **13**, 819–827 (2018).
29. X. Cheng *et al.*, Cell detection and counting through cell lysate impedance spectroscopy in microfluidic devices. *Lab Chip* **7**, 746–755 (2007).
30. S. J. Kim, S. H. Ko, K. H. Kang, J. Han, Direct seawater desalination by ion concentration polarization. *Nat. Nanotechnol.* **5**, 297–301 (2010).
31. P. Löper *et al.*, Analysis of the temperature dependence of the open-circuit voltage. *Energy Procedia* **27**, 135–142 (2012).
32. M. Zhang, N. Llaser, Investigating a micro Pirani gauge for multi-function sensing. *IEEE Sens. J.* **16**, 8062–8069 (2016).
33. X. Wang, C. Liu, Z. Zhang, S. Liu, X. Luo, A micro-machined Pirani gauge for vacuum measurement of ultra-small sized vacuum packaging. *Sens. Actuators A* **161**, 108–113 (2010).
34. X. Guo, A. Mandelis, B. Zinman, Noninvasive glucose detection in human skin using wavelength modulated differential laser photothermal radiometry. *Biomed. Opt. Express* **3**, 3012–3021 (2012).
35. Y. Y. Xie *et al.*, Metasurface-integrated vertical cavity surface-emitting lasers for programmable directional lasing emissions. *Nat. Nanotechnol.* **15**, 125–130 (2020).